32.0 ALGORITHMIC ANALYSES OF X-RADIOGRAPHY AND COMPUTED TOMOGRAPHY FOR MULTISCALE STRUCTURAL INVESTIGATIONS OF METALS (LEVERAGED)

C. Gus Becker (Mines)
Faculty: Amy Clarke (Mines)
Industrial Mentor: Michelle Espy (LANL)

This project initiated in Fall 2017 and is supported by Los Alamos National Laboratory (LANL). The research performed during this project will serve as the basis for a Ph.D. thesis program for C. Gus Becker and is supported by Los Alamos National Laboratory, the Office of Naval Research (ONR), and the US DOE National Nuclear Security Agengy (NNSA).

32.1 Project Overview and Industrial Relevance

X-ray radiography, or x-radiography, allows for the imaging of materials in a non-destructive manner by observing x-rays transmitted through the material. This method can be used for post-mortem analysis, as well as in-situ imaging of microstructural development. For example, dynamic imaging of microstructural evolution during processing (e.g. casting or directional solidification) can further our understanding of the mechanisms driving microstructural development, improving predictive capabilities [32.1]. X-radiography can also be used to capture multiple images of a sample from different angles, which can be reconstructed and represented as a three-dimensional model. A reconconstruction of a metal sample created with additive manufacturing (AM) can be generated to reveal microstructural characteristics and internal defects. Reconstructions can also be created from four-dimensional microscopy (three spatial and one temporal dimension), in which images are collected from different angles of a time-evolving sample. These reconstructions are created using techniques like Time-Interlaced Model-Based Iterative Reconstruction (TIMBIR) [32.2], which improves temporal resolution to capture microstructural evolution during processing.

Synchrotron x-ray sources can be used to obtain high-spatial resolution x-ray radiographs (on the order of 1 μm), however these images have small fields of view and require beam time at national user facilities. High-energy microfocus x-radiography has lower spatial resolutions, but significantly increases the field of view and can be performed in a laboratory. These laboratory instruments consist of a high-energy microfocus x-ray source, radiation shielding (typically a lead-lined cabinet housing the source), a scintillator to convert x-rays to visible light, and a camera/detector to collect the produced light. Tomographic data can be obtained when a rotation stage is included. Solidifiation experiments are often performed at synchrotron x-ray facilities like the Advanced Photon Source (APS) at Argonne National Laboratory (ANL), as well as in facilities with microfocus x-ray capabilities, including the non-destructive testing group (E-6, formerly AET-6) at LANL to study the microstructures and properties of materials. Many experiments have been performed by CANFSA faculty and students at Mines to study different aspects of alloy solidification, such as crystal growth and solute segregation [32.1], primary dendrite spacings and sizes [32.3], dendrite fragmentation [32.4], and the effect of different cooling rates on solidification [32.5].

When x-radiography and computed tomography are used for the non-destructive imaging of metals, sample thickness is a constraint for high density alloys. X-rays at national user facilities (with energies of ~30 keV) can typically penetrate thin foils of material (~100 μm to ~1 mm) to image thin sections or small volumes to produce computed tomographic reconstructions [32.5]. These typically cannot be used to image thicker or larger samples, unless special high-energy beamlines are used with x-ray energies up to ~150 keV. High-energy microfocus x-ray imaging utilizes x-rays with energies of up to 250 keV and beyond, allowing sample thicknesses on the order of millimeters and larger fields-of-view on the order of centimeters. Proton radiography (pRad), in which 800 MeV energy protons are used as an incident radiation source at LANL's Los Alamos Neutron Science Center (LANSCE), allows for even larger sample sizes and the ability to probe materials with high atomic numbers. However, this comes at the cost of lower spatial resolution [32.1]. Proof-of-concept experiments of Transmission High-Energy Electron Microscopy (THEEM), in which extremely high-energy electrons (15 GeV) are transmitted through samples at the Stanford Linear Accelerator Center (SLAC) to achieve deeply penetrating electron radiography have also been demonstrated [32.6]. This method has yet to be optimized, but holds potential for

dynamic studies of high atomic number (Z) materials. The goal of this project is to establish high-energy (~160 keV), microfocus x-ray imaging in a laboratory setting at Mines, achieving capabilities between those of synchrotron x-ray facilities (i.e. ~1-2 µm spatial resolution and ~2 x 2 mm^2 fields-of-view) and pRad (~ 25 µm spatial resolution at best for the ×7 magnifier and ~17 x 17 mm^2 field-of-view, although note that the ×1 lens provides a 12 × 12 cm^2 field of view). The establishment of this system will enable new understanding of materials during/after processing through reconstruction and image analysis of x-radiography and computed tomography.

32.2 Previous Work

Prior to the start of this project, in-situ solidification of metals was studied using synchrotron x-radiography at the APS and high-energy microfocus x-radiography systems in a laboratory setting at LANL, in collaboration with E-6. Through the course of this project, image processing methods have been developed to process and analyze data from these experiments. These techniques enable qualitative and quantitative information to be extracted that describe multiscale solidification dynamics in metals.

Image processing methods have evolved from modular ImageJ macros at the beginning of the project to version-controlled Python modules and Jupyter notebooks [32.7]. These projects are hosted in private repositories on GitHub strengthening collaboration efforts within CANFSA. Processing and analysis with Python enables powerful packages to be leveraged, including scikit-image for image processing [32.8] and matplotlib for visualizations [32.9]. Jupyter notebooks serve as experimental tools and can also be finalized into documents that exhibit workflows, containing formatted text to hold notes, links, and explanations. Workflows stored in this manner are more readable, and therefore more accessible and reproducible than methods that rely solely on graphical user interfaces and scripts.

A Python-driven workflow was developed to process and analyze in-situ radiography of an Al-9.68 at% Ag alloy during soldification (**Figure 32.1**). This experiment was captured using high-energy microfocus x-radiography with E-6 at LANL using the same experimental setup as previous synchrotron x-ray experiments. Energy dispersive spectroscopy (EDS) was performed on the solidifed sample post solidification to determine the composition variation. Intensity values of the solidified structures determined from x-ray images compared with the composition of the structures from the EDS was published in 2021 (**Figure 32.2**) [32.9]. A radiograph processed to clearly show the solidified structure aligned with a backscattered electron (BSE) image and the position of the EDS scan across the sample enabled this one-to-one comparison. Even though x-radiography is a volume representation of the solidification structure and EDS is only a surface representation, the comparison still showed similar trends.

32.3 Recent Progress

Work is nearing completion on a manuscript for publication detailing two separate automated procedures for detecting and analyzing solid-liquid (S-L) interfaces during solidifcation. Each procedure was developed for data from a different experiment: an experiment simulating AM processing with a Ni alloy performed at the APS and a rapid solidification experiment with an Al-Si alloy captured using a novel dynamic transmission electron microscope (DTEM) at Lawrene Livermore National Laboratory. The procedures, written in Python and formatted within a series of Jupyter notebooks, utilize libraries including NumPy, imageio, napari, scikit-image, and SciPy.

The data from the AM simulator experiment exists as a series of images captured through time. The analysis procedure developed goes through the following steps for each desired image in the time series. First, raw radiographs (**Figure 32.3.a**) are smoothed with a Gaussian filter to reduce noise and then are subtracted from the succeeding smoothed radiograph in the time sequence (**Figure 32.3.b**). The intensity of these images are rescaled by clipping the top and bottom five percent intensities (**Figure 32.3.c**). The resulting rescaled images are denoised and inverted (**Figure 32.3.d**). An upper minimum threshold is performed to create a binary image (**Figure 32.3.e**). Finally, a skeletonization algorithm is applied to create one-pixel-wide regions (**Figure 32.3.f**). These skeletonized regions are analyzed using the function *regionprops* from scikit-image which determines the areas of each connected region. Bounding boxes of the regions can also be returned this way (**Figure 32.4**). Across the

experiment, the skeletonized region with the largest area consistenly corresponds to the S-L interface (**Figure 32.5**). The interfaces identified in this way match the manually identified interfaces (**Figure 32.6**). These results are being used to determine solid-liquid interface velocites under additive manufacturing conditions. Complementary modeling is being used to determine thermal gradients. Together, these results are informing analytical solidification modeling and comparisions to solidificaiton theory.

The data from the DTEM solidification experiment exists as nine temporal frames in a single image (**Figure 32.7**). To analyze the S-L interface over time, each frame is separated from the image by taking the upper minimum thresholda and cropping to the bounding box of each connected region (corresponding to a separate frame). Padding is added as necessary to ensure that each image is the same size, while aligning the frame centroids. For each frame, a pseduo-flat field image is generated using a large-kernel Gaussian filter and replacing low intensity portions of the resulting, highly-blurred image with the mean intensity of the frame. These pseudo flat-field images are used to normalize each frame, reducing intenisty fluctuations between frames (**Figure 32.8**). A series of morphological operations on the rescaled frames yield a binary image, or mask, denoting one roughly elliptical melt pool region per frame. Ellipse parameters (centroid, major axis, minor axis, and rotation) are calculated for an ellipse with an equivalent second moment. At this point, we have an ellipse that is close to matching the S-L interfaces. Each of these ellipses serve as a starting point for an optimization process, utilizing a custom cost function. The parameters of a better fitting ellipse are determined through iteration by minimizing the cost function, which returns a cost value calculated by the sum of pixels shared between the fitted ellipse and melt pool mask (**Figure 32.9**). After optimization, the fitted ellipses show a good match with the S-L interfaces in the frames. This is visible when each ellipse is overlaid on the corresponding frame (**Figure 32.10**). The solidification velocity is calculated from these fitted ellipses by fitting a first-order polynomial to the width of the ellipses plotted (along each axis) against time. The velocity is represented by the first-order coefficient of this polynomial, and is found to be 2.10 m/s along the major axis and 1.61 m/s along the minor axis of the ellipses (**Figure 32.11**). These results, along with complementary nanoscale crystallographic mapping, are being used to fundamentally understand grain competition during rapid solidification and are informing state-of-the-art phase-field predicitons with a new model develed by Karma et al. at Northeastern University to develop predictive capability of microstructure evolution at unprecedented spatial and temporal scales.

32.4 Plans for Next Reporting Period

In the next reporting period, the following tasks will be completed:

- Complete manuscript for automated melt pool detection publication.
- Adapt segmentation method combining intensity, edge, and shape information from literature to mock HE crystals (**Figure 32.12**), supported by the US DOE NNSA.

32.5 References

[32.1] P.J. Gibbs, S.D. Imhoff, C.L. Morris, F.E. Merrill, C.H. Wilde, P. Nedrow, F.G. Mariam, K. Fezzaa, W.K. Lee, A.J. Clarke, Multiscale X-ray and proton imaging of bismuth-tin solidification, JOM. 66 (2014) 1485–1492. https://doi.org/10.1007/s11837-014-1058-0.

[32.2] K.A. Mohan, S. V. Venkatakrishnan, J.W. Gibbs, E.B. Gulsoy, X. Xiao, M. De Graef, P.W. Voorhees, C.A. Bouman, TIMBIR: A Method for Time-Space Reconstruction From Interlaced Views, IEEE Trans. Comput. Imaging. 1 (2015) 96–111. https://doi.org/10.1109/TCI.2015.2431913.

[32.3] A.J. Clarke, D. Tourret, Y. Song, S.D. Imhoff, P.J. Gibbs, J.W. Gibbs, K. Fezzaa, A. Karma, Microstructure selection in thin-sample directional solidification of an Al-Cu alloy: In situ X-ray imaging and phase-field simulations, Acta Mater. 129 (2017) 203–216. https://doi.org/10.1016/j.actamat.2017.02.047.

[32.4] J.W. Gibbs, D. Tourret, P.J. Gibbs, S.D. Imhoff, M.J. Gibbs, B.A. Walker, K. Fezzaa, A.J. Clarke, In Situ X-Ray Observations of Dendritic Fragmentation During Directional Solidification of a Sn-Bi Alloy, JOM. 68 (2016) 170–177. https://doi.org/10.1007/s11837-015-1646-7.

[32.5] B.M. Patterson, K.C. Henderson, P.J. Gibbs, S.D. Imhoff, A.J. Clarke, Laboratory micro- and nanoscale X-ray tomographic investigation of Al-7 at.%Cu solidification structures, Mater. Charact. 95 (2014) 18–26. https://doi.org/10.1016/j.matchar.2014.06.004.

[32.6] F. Merrill, J. Goett, J. Gibbs, S. Imhoff, F. Mariam, C. Morris, L. Neukirch, J. Perry, D. Poulson, R. Simpson, P.L. Volegov, P.L. Walstrom, C. Hast, K. Jobe, T. Smith, U. Wienands, A.J. Clarke, D. Tourret, Demonstration of Transmission High Energy Electron Microscopy, (2017) 1–10.

[32.7] S. van der Walt, J.L. Schönberger, J. Nunez-Iglesias, F. Boulogne, J.D. Warner, N. Yager, E. Gouillart, T. Yu, scikit-image: image processing in Python, PeerJ. 2 (2014) e453. https://doi.org/10.7717/peerj.453.

[32.8] J.D. Hunter, Matplotlib: A 2D graphics environment, Comput. Sci. Eng. 9 (2007) 90–95. https://doi.org/10.1109/MCSE.2007.55.

[32.9] C.G. Becker, D. Tourret, D. Smith, B. Rodgers, S. Imhoff, J. Gibbs, J. Hunter, M. Espy, K. Clarke, A. Clarke, Integrating In Situ x-Ray Imaging, Energy Dispersive Spectroscopy, and Calculated Phase Diagram Analysis of Solute Segregation During Solidification of an Al-Ag Alloy, JOM. (2021). https://doi.org/10.1007/S11837-021-04884-8.

[32.10] C. Wälhby, I.M. Sintorn, F. Erlandsson, G. Borgefors, E. Bengtsson, Combining intensity, edge and shape information for 2D and 3D segmentation of cell nuclei in tissue sections, J. Microsc. 215 (2004) 67–76. https://doi.org/10.1111/J.0022-2720.2004.01338.X.

32.6 Figure and Tables

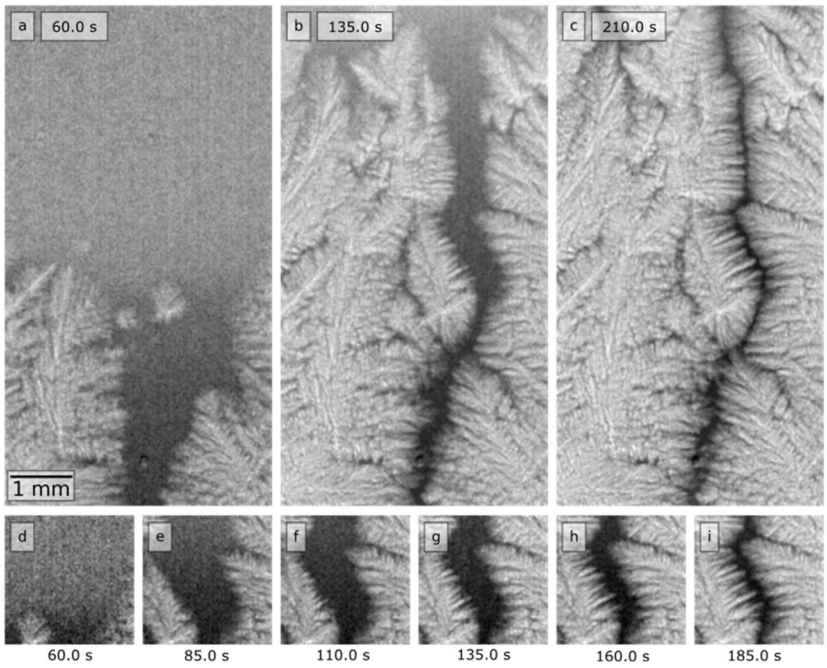

Figure 32.1: (a – c) In situ x-radiographs showing the mesoscale solidification of an Al-9.68 at% Ag sample, with time shown in seconds passed since the start of solidification within the viewing window. (d – i) Additional frames for a region of interest in the middle right of the full sample. Lighter regions are Al-rich, whereas darker regions are Ag-rich.

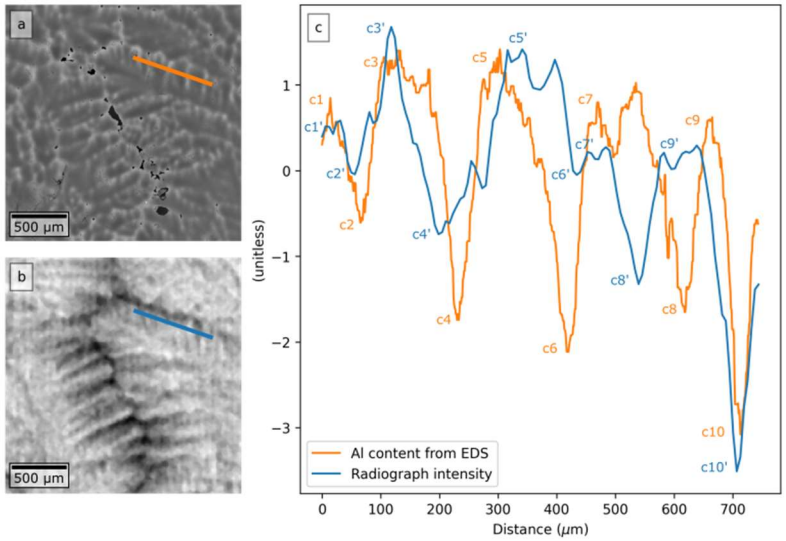

Figure 32.2: (a) BSE image of an Al-Ag sample, showing the position of an EDS line scan measuring the Al content. (b) X-radiograph of the same sample region. (c) Al content from the EDS line scan (orange) and the transmitted x-ray intensity (blue) collected across the length of the lines in a and b, respectively. Each dataset is standardized to a unitless range for comparison. EDS features annotated as c1-10 correlate to x-radiography features annotated as c1'-10' respectively.

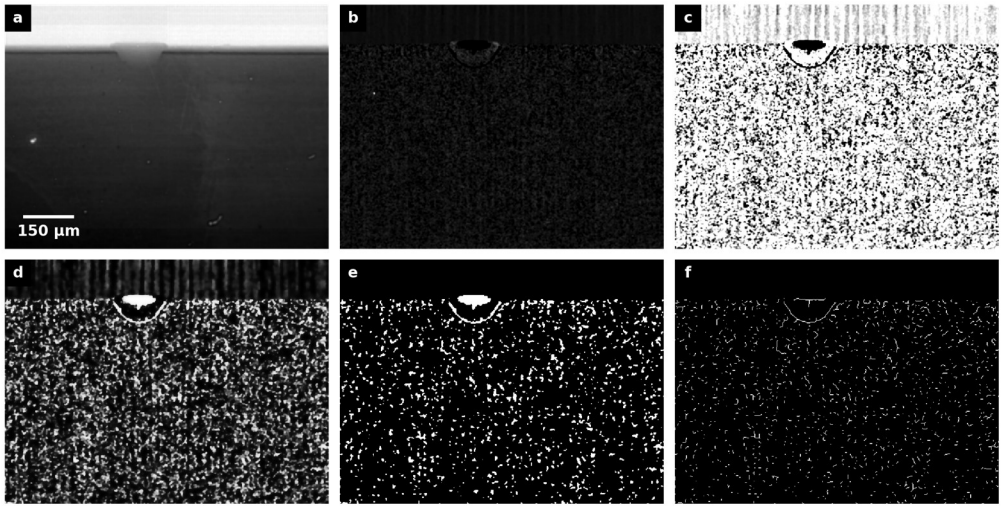

Figure 32.3: The procedural image processing routine for identifying the solid-liquid (S-L) interface for a radiograph taken during the solidification portion of an APS simulated additive manufacturing experiment just after laser melting. a) Raw radiograph showing the melt pool and S-L interface. b) Smoothing with a Gaussian filter and subtraction from the succeeding smoothed radiograph in the time sequence. c) Intensity rescaling by clipping the top and bottom five percent intensities. d) Denoising and intensity inversion. e) Upper minimum threshold to convert to binary image. f) Skeletonization to create one-pixel wide regions.

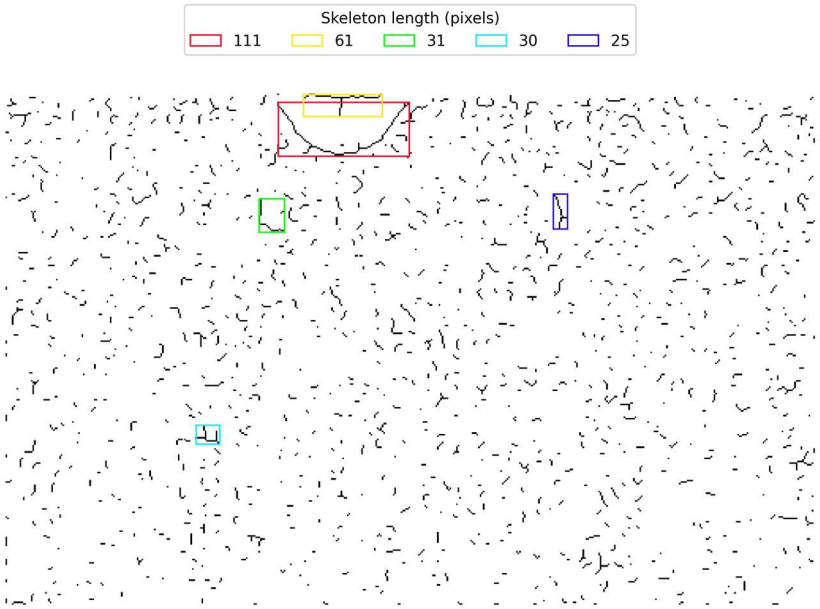

Figure 32.4: Skeletonized image showing the bounding box of the five largest skeletons. In order of largest pixel area/length to smallest: red, yellow, green, cyan, violet.

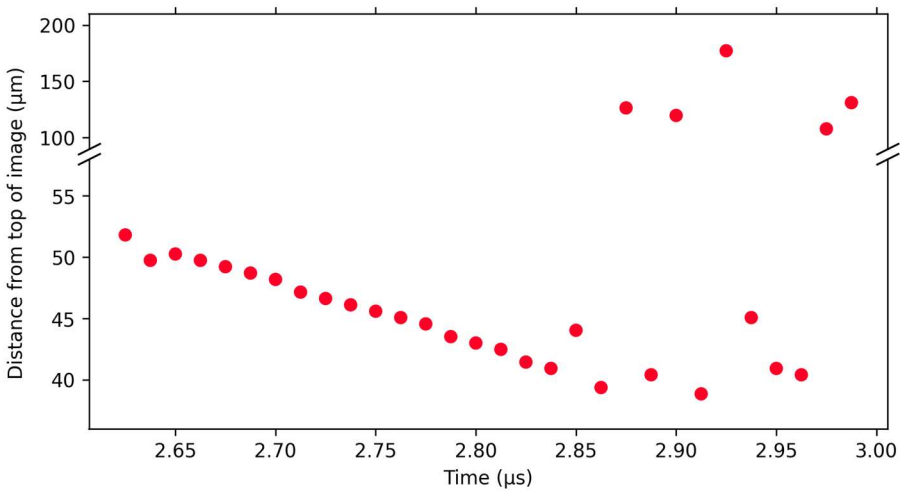

Figure 32.5: Distance of bottom of solid-liquid interface from the top of the image, as detected by the identification routine. Note that the outliers beyond 2.85 μs are plotted with a different y-axis scale.

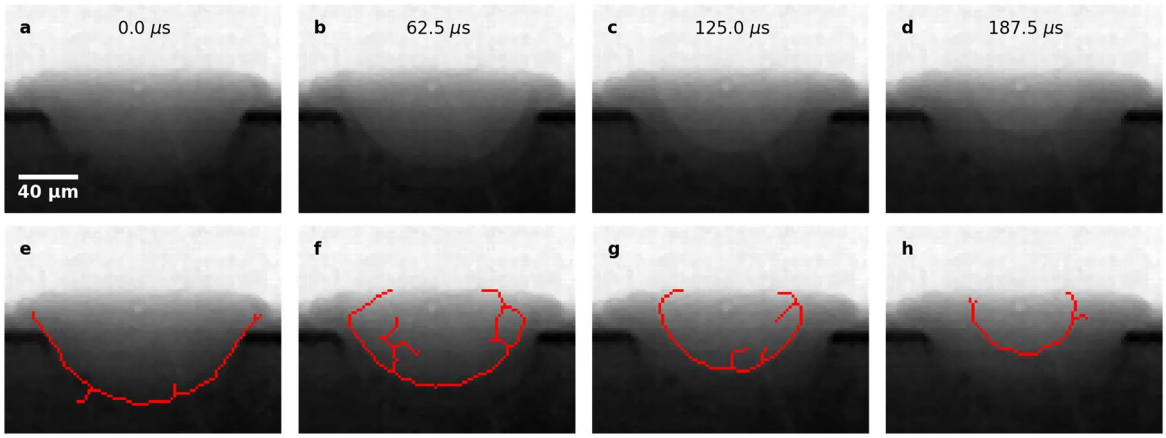

Figure 32.6: (a – d) Subset of radiography sequence showing the solid-liquid interface receding throughout the experiment. (e – f) Skeletonized regions overlaid in red on subset of radiography sequence showing the as-detected position of the solid-liquid interface throughout the experiment.

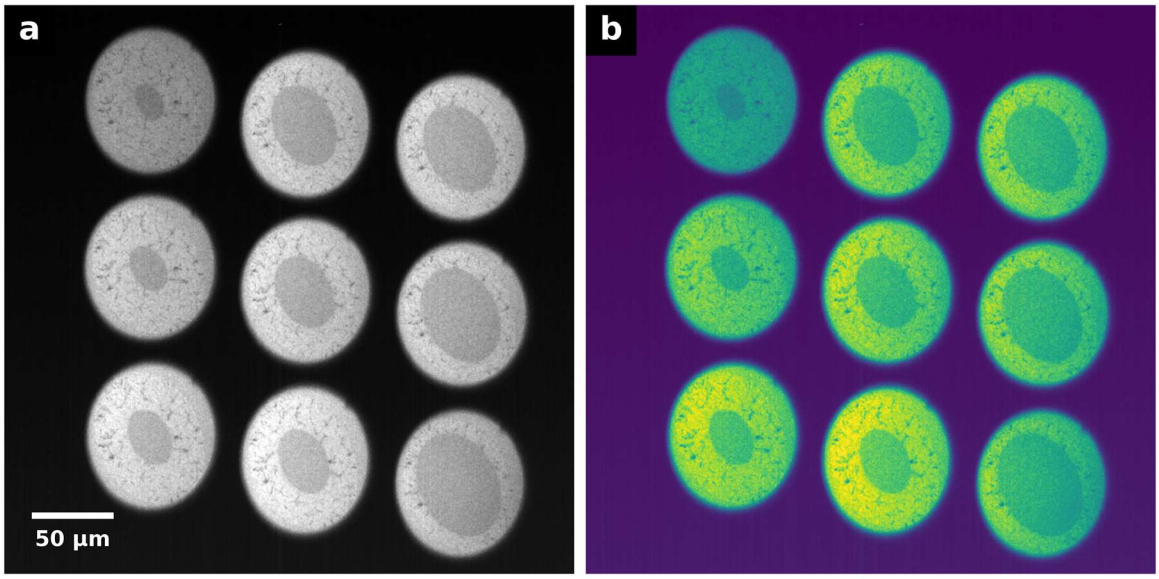

Figure 32.7: (a) Dynamic Transmission Electron Microscope (DTEM) image showing nine frames of a rapidly solidifying Al-3 Si sample with a 20 µs delay and 2.5 µs capture interval. The chronology of the experiment starts with the lower right image, moves up the right column, down the center column, and finally up the left column to end at the top left image. (b) The same image with false color highlighting intensity differences across the image.

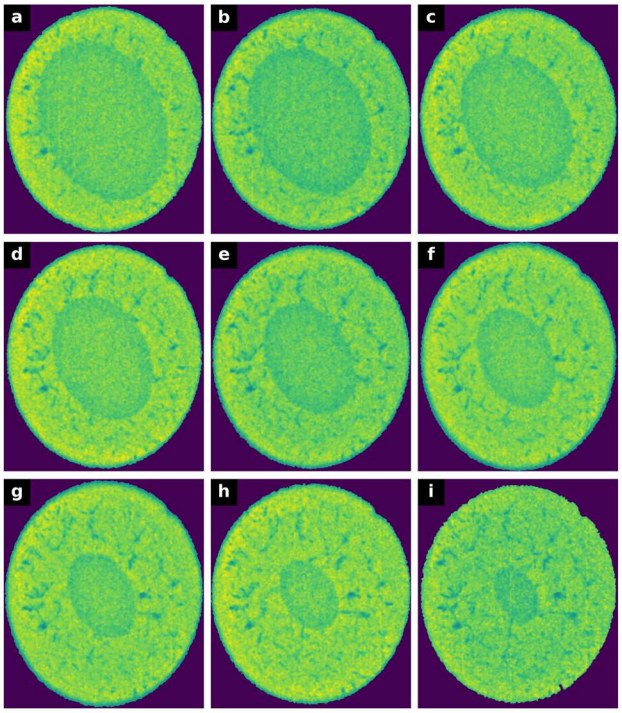

Figure 32.8: Frames from DTEM image separated, ordered chronologically, and rescaled via pseudo flat-field correction.

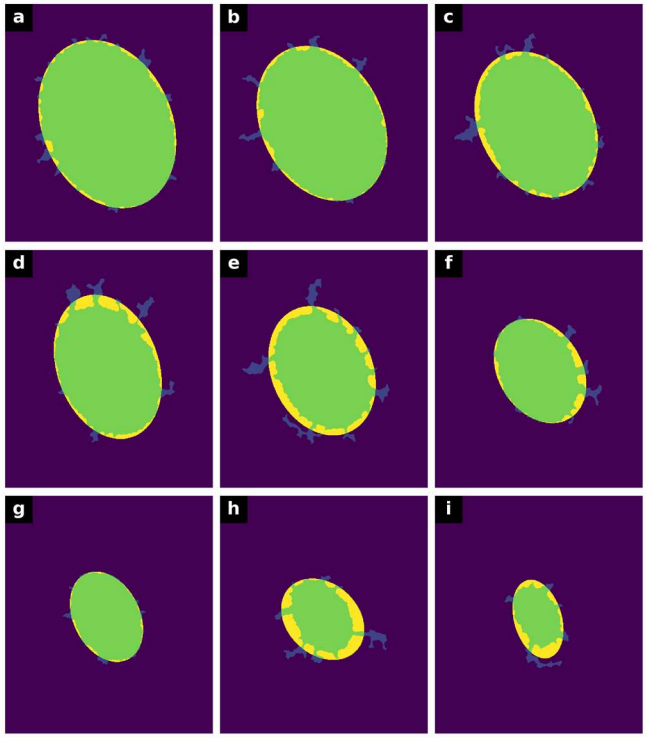

Figure 32.9: Fit mismatch shown for ellipses with the same second moment as the melt pool masks. Mismatch shown by true positive match (green), false positive match (yellow), and false negative match (blue).

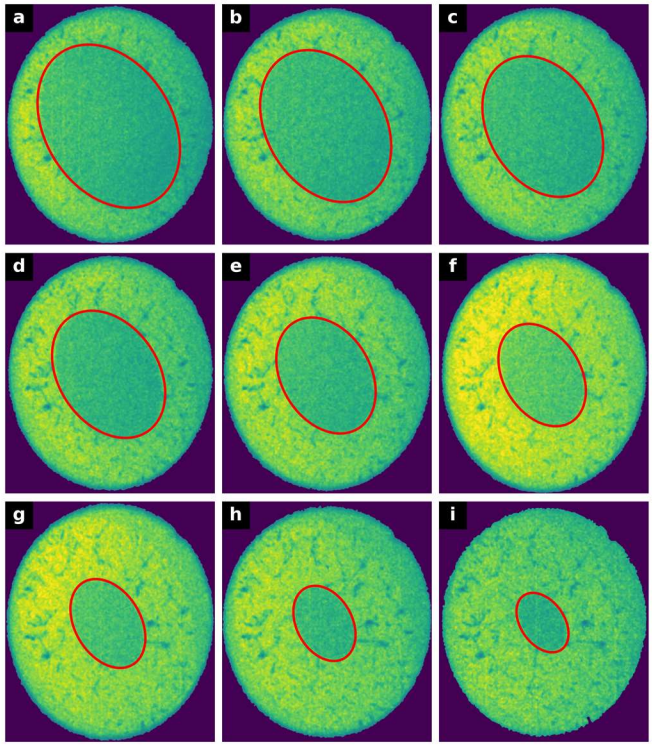

Figure 32.10: Fitted ellipses following optimization through cost minimization overlaid in red on corresponding frames.

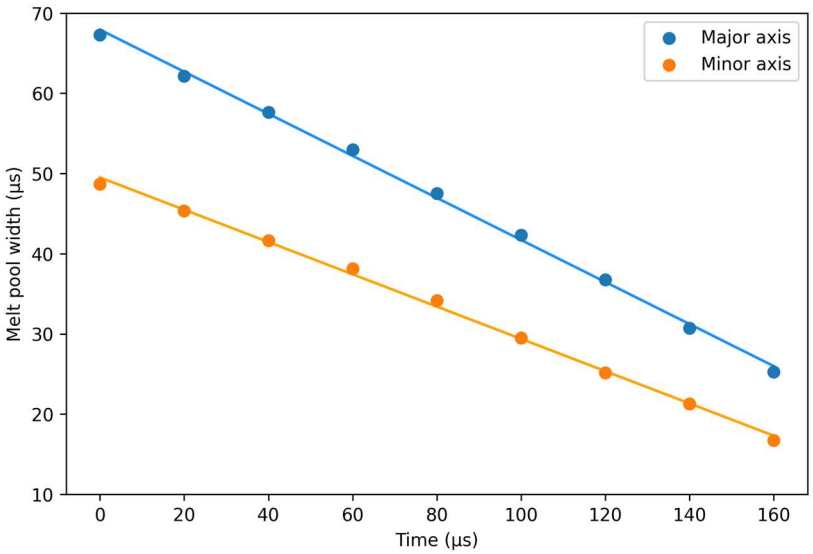

Figure 32.11: Size of melt pools over time from the major (blue) and minor (orange) axes of the fitted ellipses. Solidification velocity is determined by fitting a first-order polynomial and selecting the first-order coefficient. This yields 2.10 m/s along the major axes and 1.61 m/s along the minor axes.

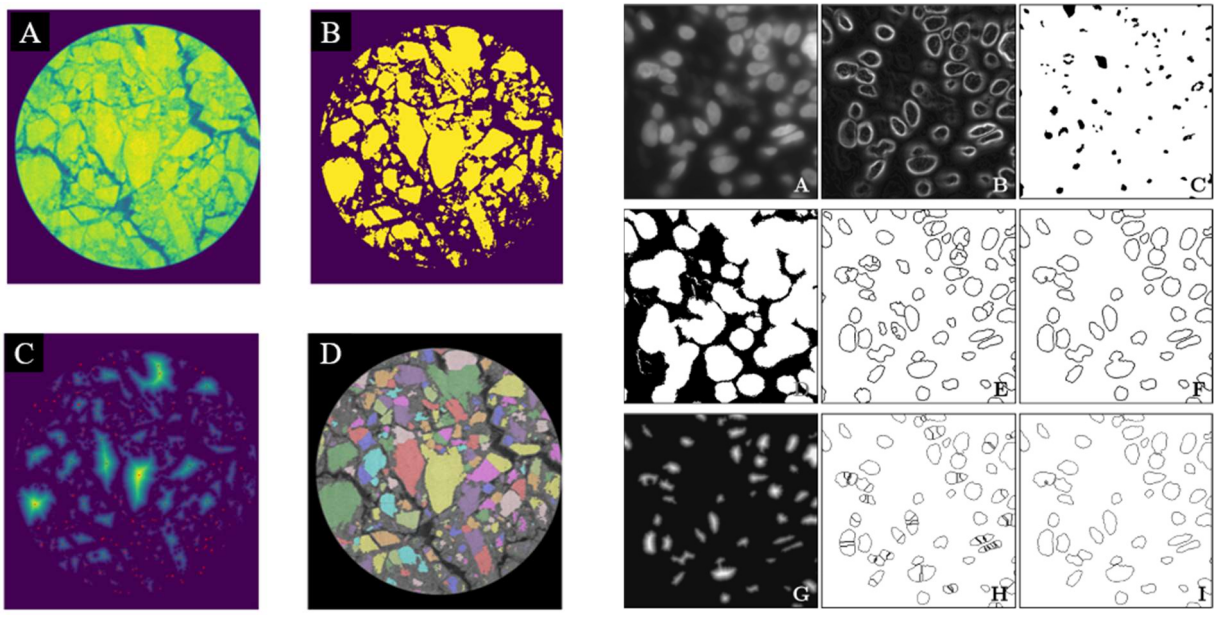

(a) (b)

Figure 32. 11: (a) Current method of segmenting mock HE crystals from surrounding binder. A: Original image. B: Threshold at manually chosen value. C: Create distance map and identify local maxima. D: Watershed segmentation with local maxima as seeds. (b) Method of C. Wälhby et al. [32.10] for segmentation that combines intensity, edge, and shape information. A: Original fluorescence microscopy image slice of a tumor. B: Gradient of A. C: Foreground seeds from local maxima. D: Background seeds from local maxima of B (with removal of small components). E: Seeded watershed segmentation. F: Merging of seeded objects based on edge strength. G: Distance map of E. H: Watershed segmentation of distance transform before merging. I: Final segmentation result based on intensity, edge, and shape information.